



Macro modeling of ion sensitive field effect transistor with current drift



Dae Woong Kwon^a, Sihyun Kim^a, Ryoongbin Lee^a, Hyun-Sun Mo^b, Dae Hwan Kim^b,
Byung-Gook Park^{a,*}

^a Department of Electrical and Computer Engineering and Inter-university Semiconductor Research Center, Seoul National University, Seoul 151-742, Republic of Korea

^b School of Electrical Engineering, Kookmin University, Seoul 136-702, Republic of Korea

ARTICLE INFO

Article history:

Received 15 October 2016

Received in revised form 23 February 2017

Accepted 21 March 2017

Available online 28 March 2017

Keywords:

ISFET with CMOS circuit

Drift effect mechanism

Drift effect modeling

Macro model of ISFET

Circuit model of ISFET

ABSTRACT

In terms of the application of the ion sensitive field effect transistor (ISFET) fabricated with top-down approached and CMOS-compatible back-end process to integrated circuits, the macro model of the ISFET is required. Although several models have been reported, there is no electrical model that reflects the time-dependent drain current (I_D) change (drift effect). We propose the electrical model which can reflect the drift effect and can be expressed by the combination of electrical circuit components. In the proposed model, R_1 represents the resistance of the electrolyte and the FET can be approximated by the capacitances C_1 (capacitance of pure gate oxide in which hydrogen ions move very slowly) and C_2 (capacitance by gate oxide with defects in which hydrogen ions move relatively faster). Furthermore, the movement of hydrogen ions in the defective oxide is represented by R_2 and the current drift is modeled as the parallel combination of the C_2 and the R_2 because the drift effect is strongly related to hydrogen ion movement through defective gate oxide or Helmholtz layer. Consequently, the ISFET with the I_D drift can be modeled by the series connection of the R_1 , the parallel combination of the C_2 and the R_2 , and the C_1 . Also, The I_D calculated by the proposed model is successfully fitted to the measured time-dependent I_D of the ISFET.

© 2017 Elsevier B.V. All rights reserved.

1. Introduction

As fabrication technology has continued to develop, various nano-size biomedical sensors have been widely researched since the size of biological entities, such as DNA, proteins, and viruses are similar to their size [1,2]. Especially, biomedical sensors using fluorescent labeling and parallel optical detection techniques have received much attention for high sensitivity [3]. However, they have a number of drawbacks such as expensive and time-consuming processes for sample preparation and data analysis. To overcome these limitations, silicon nanowire (SiNW) Ion Sensitive Field Effect Transistors (ISFET) have been proposed as one of the most promising biomedical sensors since it has good characteristics such as label-free, real-time detection, and excellent sensitivity caused by high surface-to-volume ratio [4].

In terms of the fabrication process, the early stage of SiNW biosensors had been studied through a bottom-up approach [5–8]. However, the bottom-up approach has serious disadvantages in

the reproducibility of fabrication process and device design since it is difficult to control doping concentration and dimension parameters which affect the electrical performance of the device. Also, it is not suitable to be integrated with mature complementary metal-oxide semiconductor (CMOS) technology and circuitry because SiNWs fabricated by the bottom-up process cannot be well-aligned with electrodes. Meanwhile, a top-down approach can produce uniformly distributed and well-aligned NWs in pre-determined orientation and position on substrate. Thus, many researchers have demonstrated CMOS-compatible biosensors by using top-down processed NWs [9–18]. Although the possibility of the integration with mature state-of-the-art CMOS technology and circuitry has been argued in the previous works on the top-down CMOS-compatible biosensors, the real integration of top-down approached SiNW biosensors with CMOS technology and circuit has been rarely reported. Furthermore, most previous works have adopted the lift-off process which is not compatible with the conventional CMOS back-end process. Thus, for assessing real advantages of SiNW-CMOS hybrid systems and expediting their wafer-scale mass-productions, the SiNW biosensors should be integrated with CMOS circuits by using the back-end process compatible with the conventional CMOS technology. Recently,

* Corresponding author.

E-mail address: bgpark@snu.ac.kr (B.-G. Park).

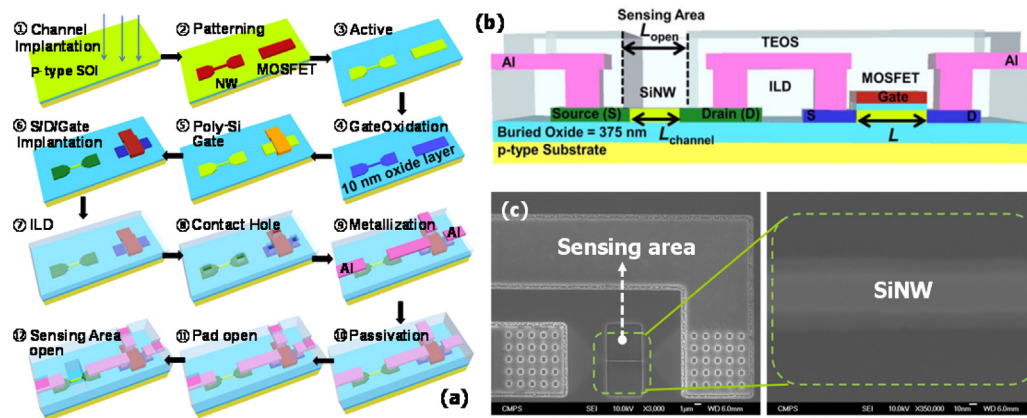


Fig. 1. (a) Fabrication process of SiNW sensor with MOSFET. (b) Schematic diagram of SiNW sensor with MOSFET. (c) Top view SEM image of fabricated SiNW sensor.

our group demonstrated a novel high-sensitive SiNW biosensor which was co-integrated with CMOS circuit by using top-down approached and CMOS-compatible back-end process simultaneously [19,20]. However, there are still challenges on the path to commercialization as chemical and biomedical sensors. Particularly, the current drift (change of drain current under a fixed bias as a function of measurement time) has been considered to be one of the critical obstacles because it is almost impossible to read precise current value within limited sensing time [21].

In the view point of the application of the co-integrated ISFET with CMOS circuit, the macro model of the ISFET including the current drift should be introduced to estimate the sensing performance of the ISFET-CMOS hybrid system as a function of time and to find a solution for the drift effect. A basic electrical model was demonstrated in [22] by considering only electrostatic state and thus the time dependence of sensing current (namely, current drift) cannot be expressed. The improved model considering the drift effect was reported in [23]. However, the drift model is based on a physical method. Therefore, in this study, we propose the electrical model which can explain the drift mechanism and can be expressed by the combination of electrical circuit components.

2. Experimental

To verify the proposed macro modeling including the drift effect, SiNW sensors were co-integrated with CMOS circuit by using top-down approached and CMOS-compatible back-end process. The detailed fabrication process is illustrated in Fig. 1(a). The proposed devices were fabricated on $4 \times 10^{15} \text{ cm}^{-3}$ boron-doped (100) silicon on insulator (SOI) wafer (top Si layer = 100 nm and buried oxide = 375 nm). Firstly, 1) The ion implantation was conducted on the Si layer thinned to 80 nm via thermal oxidation for channel doping, p-region (dopant: B^+ , energy: 20 keV, dose: $5 \times 10^{13} \text{ cm}^{-2}$) and n-region (P^+ 40 keV $3 \times 10^{13} \text{ cm}^{-2}$). Then, an annealing process was conducted at 950°C for 30 min for the uniform channel doping of the 80 nm thick silicon channel. 2) The active region was defined by mix-and-match process of e-beam and conventional photolithography on the silicon layer. 3) The silicon layer was dry-etched by HBr/O_2 inductively coupled plasma (ICP) for the active formation. 4) The 10 nm thick gate oxide was formed by dry-oxidation at 850°C . 5) The 100 nm thick poly-silicon was deposited at 630°C by low pressure CVD (LPCVD). The gate of the MOSFET was defined and the poly-silicon on the SiNW was removed by photolithography and ICP dry-etching. 6) By using photo resist (PR) mask which covers only the SiNW channel, the gate (G) of the MOSFET and source/drain (S/D) of both the SiNW and the MOSFET were doped by As^+ ion implantation for n-type S/D/G and BF_2^+ ion

implantation for p-type S/D/G, respectively. A rapid thermal annealing (RTA) was implemented at 900°C for 10 seconds to activate the dopants. 7) Inter-layer dielectric oxide (ILD) was deposited by high density plasma CVD (HDPCVD). 8) The contact holes were formed by photolithography and dry-etching. 9) The aluminum layer was formed on the ILD for metallization. 10) The tetraethyl orthosilicate layer was deposited for passivation. 11) The pads were opened by photolithography and dry-etching. 12) The oxide layer around the SiNW was removed by using a magnetically enhanced reactive ion etching technique in CHF_3/CF_4 plasma to define the sensing area. Finally, an alloying process was carried out. Fig. 1(b) shows the schematic of the fabricated SiNW sensor and the co-integrated MOSFET. Also, Fig. 1(c) shows the top-view SEM image of the fabricated SiNW sensor.

A polydimethylsiloxane (PDMS) fluidic channel was bonded on the fabricated chip for the fluidic transport of analyte solution as can be seen in Fig. 2(b) and (c). Then, the measurement system with tubing lines (inner diameter = $400 \mu\text{m}$, outer diameter = 1.6 mm) on a probe station was setup as depicted in Fig. 2(d). The schematic diagram for the measurement setup using the PDMS fluidic channel is shown in Fig. 2(e). Here, the gate voltage (V_{LG}) of the SiNW sensor is applied to the liquid gate through the Ag/AgCl reference electrode (RE). The fabricated devices were functionalized using 3-aminopropyl-triethoxysilane (APTES) to obtain an amine ($-\text{NH}_2$) surface. 0.1 M potassium dihydrogen phosphate (KH_2PO_4) and potassium monohydrogen phosphate (K_2HPO_4) were used to control the buffer solutions with HCl and KOH.

3. Results and discussion

3.1. Mechanism of current drift

The fabricated SiNW sensor and MOSFET were characterized with a semiconductor parameter analyzer (4156C, Agilent) at room temperature. Fig. 3(a) and (b) show the drain current (I_{D})– V_{LG} curves of the n-type SiNW sensor and the I_{D} –gate voltage (V_{G}) curves of the n-type/p-type MOSFETs, respectively. It is confirmed that the SiNW sensor is co-integrated successfully with the CMOS circuit by using top-down approached and CMOS-compatible back-end process.

Fig. 3(c) indicates the measured transfer characteristics of the SiNW sensor for different pH solutions. Through the measurements, the clear modulation of the I_{D} with changing pH values is verified. Fig. 3(d) demonstrates that the threshold voltage shift (ΔV_{th}) is obtained to be $\Delta V_{\text{th}} = \sim 50 \text{ mV/pH}$ for the n-type SiNW sensor, which confirms that the surface potential at the SiO_2/SiNW interface is well modulated by pH values. However, Fig. 4(b) and (c) show that the I_{D} is increased (namely, I_{D} drift) throughout the mea-

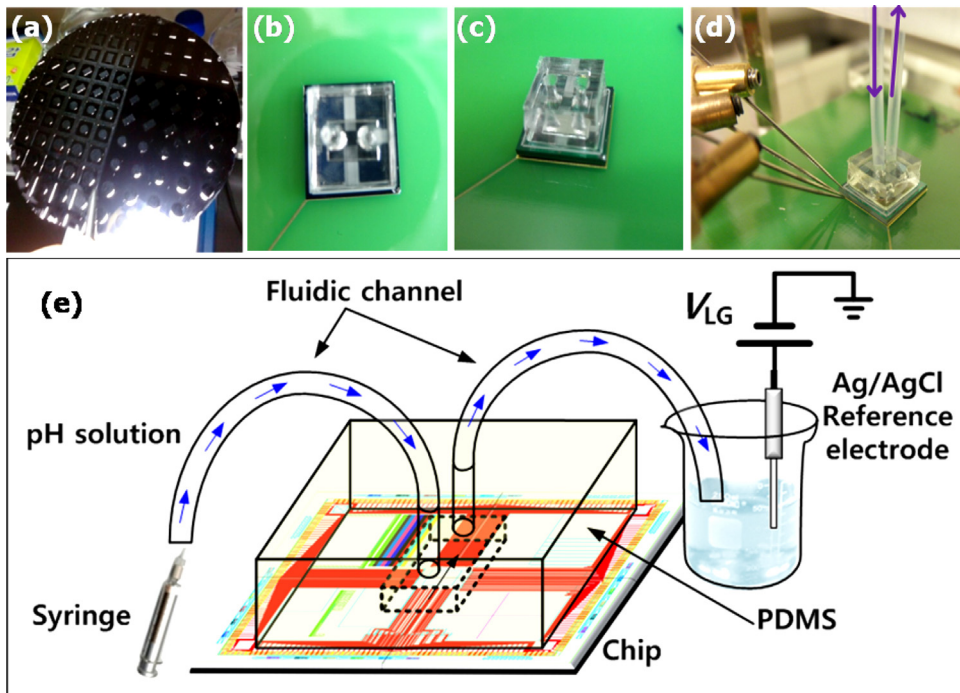


Fig. 2. (a) Fabricated PDMS channel master on 4-inch Si wafer. (b) Top view and (c) bird's eye view of PDMS channel attached to fabricated chip. (d) Measurement setup with tube. (e) Schematic diagram of entire measurement system.

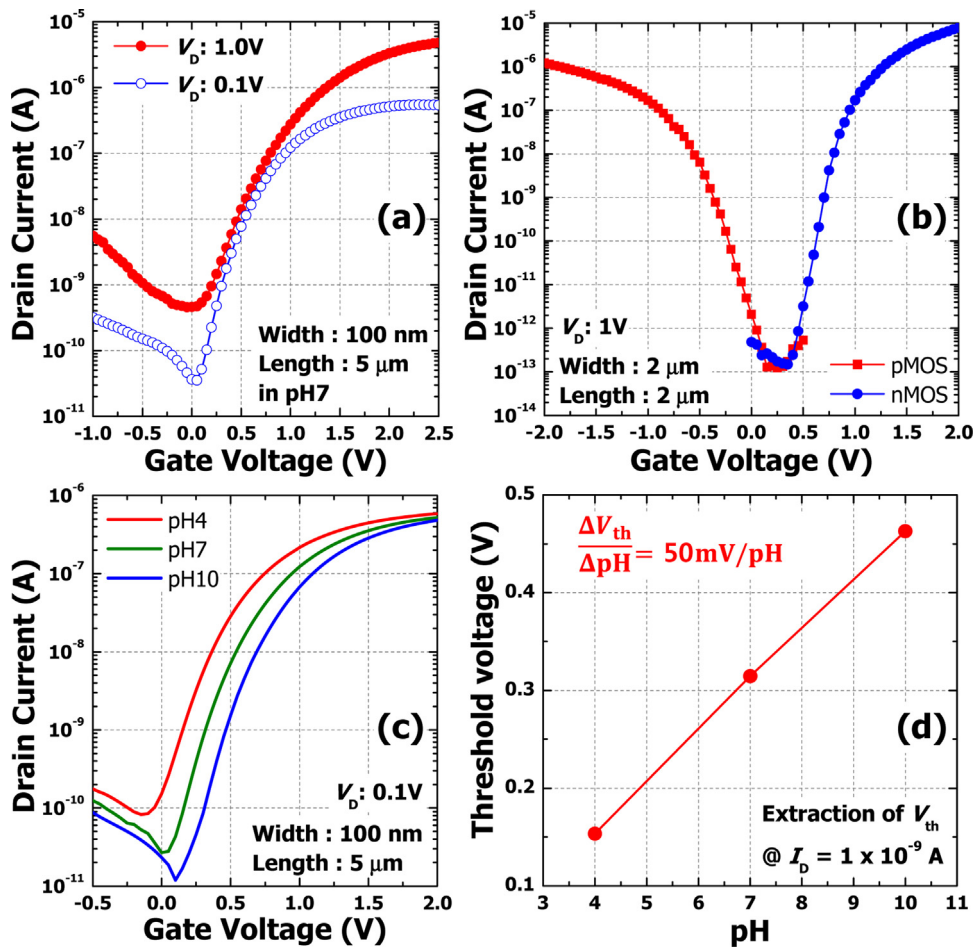


Fig. 3. Measured (a) drain current (I_D)-liquid gate voltage (V_{LG}) curves of n-type SiNW sensor and (b) I_D -gate voltage (V_G) curves of n-type/p-type MOSFETs, respectively. (c) Transfer characteristics of n-type SiNW sensor according to pH level. (d) Change of threshold voltage (V_{th}) by pH variation. All V_{th} s were extracted by constant current method at $1 \times 10^{-9} A$.

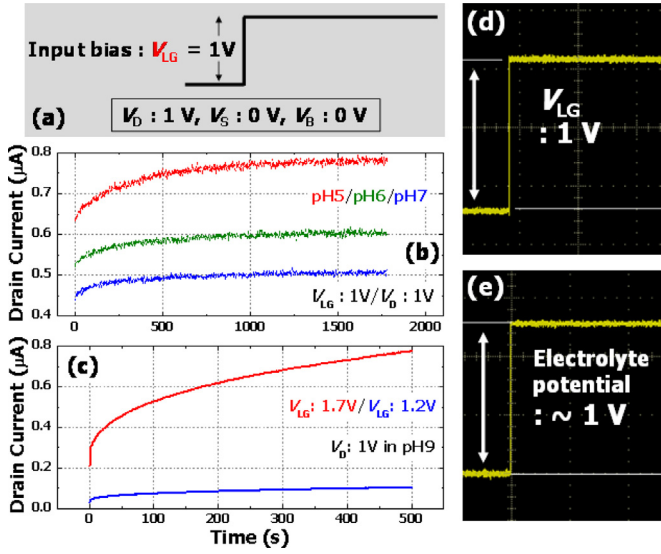


Fig. 4. (a) Input pulse applied to liquid gate through reference electrode. (b) Transient characteristics of I_D under condition of $V_{LG} = 1\text{ V}$ and $V_D = 1\text{ V}$ in various pH solutions. (c) Transient characteristics of I_D measured by various V_{LG} s in pH 9 solution. (d) Bias voltage applied to reference electrode. (e) Bias voltage measured from the electrolyte in pH 8 solution.

surement time (T_M). The I_D increase rapidly in a few seconds at first (fast response). After that, the I_D increase slowly until $\sim 1700\text{ s}$ (slow response). The biases of Fig. 4(a) were applied for the measurement of the I_D drift.

Considering 300 K was maintained during the entire measurement, the effect of temperature on the I_D drift can be ignored. To check if the RE potential drifts, two REs (main and auxiliary) were employed. A second (auxiliary) electrode was immersed inside the electrolyte of Fig. 2(e) with some distance from the reference electrode (main). The V_{LG} of Fig. 4(d) was applied to the main RE, and the electrolyte potential was measured through the auxiliary RE by high input impedance electrometer. Fig. 4(d) and (e) indicate that I_D still drifts although the potential of the electrolyte completely follows the bias voltage applied to the RE without any drift. Based on these results, it is clearly confirmed that the observed slow I_D drift should be attributed to the potential change at Helmholtz layer (HL) or the sensing oxide. The physical origin of the slow response can be explained by hydrogen ion (H^+) injection into defective sensing oxide [21]. To clarify the correlation between the H^+ injection and the I_D drift, the transient characteristics of I_D were measured at different V_{LG} s and in various pH solutions. Fig. 4(b) demonstrates that I_D drifts more as the pH of the solution decreases (meaning that H^+ concentration in the solution increases) at V_{LG} of 1 V. Also, as shown in Fig. 4(c), the I_D drift gets accelerated by the higher V_{LG} in pH 9 solution. These results strongly support that field enhanced H^+ movement through the sensing insulator causes the I_D drift [24,25]. Furthermore, considering the diffusion constants of H^+ (D_{ox-H^+}) in pure oxide and defective oxide, it can be simply noticed that the H^+ movement mainly occurs in the defective oxide. The D_{ox-H^+} in pure oxide is much lower than that in oxide with defects (D_{ox-H^+} in defective oxide $\sim 10^{-18}\text{ cm}^2/\text{s}$, D_{ox-H^+} in pure oxide $\sim 10^{-23}\text{ cm}^2/\text{s}$). It means that H^+ cannot move through the pure oxide (Diffusion length in pure oxide is 0.2 nm per a year), whereas H^+ can be diffused in the defective oxide although the process is slow. Consequently, the I_D is continuously increased during the T_M because the penetration of H^+ into the defective oxide is accelerated by V_{LG} and the injected H^+ is diffused toward the channel of the n-type SiNW sensor as shown in Fig. 5(a). Additionally, Fig. 5(b) shows that the bi-layer of pure oxide and defective oxide can be formed in our fabricated SiNW sensor by the plasma dam-

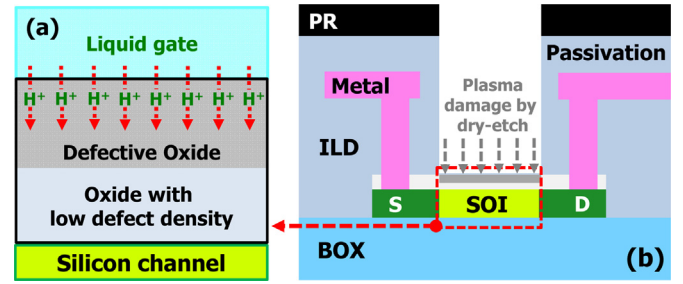


Fig. 5. (a) Hydrogen ion (H^+) penetration from liquid gate accelerated by V_{LG} . (b) Cross-sectional image of SiNW sensor in sensing area opening process of Fig. 1(a), which explains that defective oxide can be generated by plasma damage induced by dry-etching.

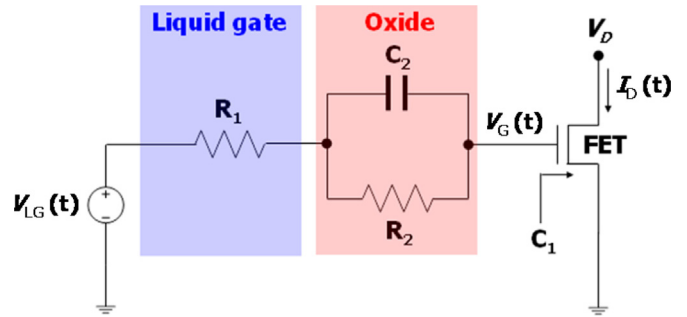


Fig. 6. A schematic model including drift effect. It is composed of only electrical components.

age during the sensing area open process of Fig. 1(a). As long as the sensing area is formed by a dry etching process, the formation of the defective oxide is inevitable. However, even if it is assumed that the defective oxide is not formed during the dry etching process, the interface of the sensing oxide become defective due to the chemical modification induced by the surface reaction between liquid gate and the sensing oxide [26,27].

3.2. Macro model of ISFET with current drift

To model the I_D drift induced by the H^+ movement, we set up a simple circuit as shown in Fig. 6 where R_1 represents the resistance of the electrolyte and the FET can be approximated as capacitances, C_1 and C_2 . C_2 is the capacitance by gate oxide with defects in which the hydrogen ions move relatively faster than those of pure oxide. C_1 is the capacitance of the pure oxide in which the hydrogen ions move very slowly. R_2 represents the ion movement through the defective oxide. The low diffusion constant in the oxide causes the bottleneck of the ion motion. The slow movement of hydrogen ions in the defective oxide is modeled as the parallel combination of the C_2 and the large resistance R_2 . In the model, the V_{LG} is applied as a unit step function and the input loop is considered for the analysis of the response to the V_{LG} .

According to Kirchhoff's law, we can get the two equations, Eq. (1) and (2) about V_{LG} and current (I) flowing from the liquid gate toward the gate oxide.

$$V_{LG}(t) = R_1 I + V_2 + \frac{1}{C_1} \int_0^t I dt \tag{1}$$

$$I = C_2 \frac{dV_2}{dt} + \frac{V_2}{R_2} \tag{2}$$

where V_2 is the voltage across the defective oxide. As Eq. (2) is substituted into Eq. (1), the V_{LG} is expressed by the circuit components, C_1, C_2, R_1, R_2 and V_2 . The expression is given by

$$V_{LG}(t) = R_1 C_2 \frac{dV_2}{dt} + \frac{R_1}{R_2} V_2 + V_2 + \frac{C_2}{C_1} V_2 + \frac{1}{C_1 R_2} \int_0^t V_2 dt' \quad (3)$$

By using Laplace transform for $V_{LG}(t) = Vu(t)$, Eq. (3) is given by

$$\frac{V}{s} = R_1 C_2 s V_2 + \left[\frac{R_1}{R_2} + \frac{C_2}{C_1} + 1 \right] V_2 + \frac{1}{C_1 R_2 s} V_2 \quad (4)$$

$$C_1 R_2 V = [C_1 C_2 R_1 R_2 s^2 + (C_1 R_1 + C_2 R_2 + C_1 R_2) s + 1] V_2 \quad (5)$$

$$V_2 = \frac{C_1 R_2}{C_1 C_2 R_1 R_2 s^2 + (C_1 R_1 + C_2 R_2 + C_1 R_2) s + 1} V \quad (6)$$

Furthermore, I can be expressed by Laplace transform of Eq. (2) as follows.

$$I = (C_2 s + \frac{1}{R_2}) V_2 \quad (7)$$

From the schematic model of Fig. 6, Laplace transformed Eq. (8) is obtained. As Eq. (6) and Eq. (7) are substituted into Eq. (8), the V_1 is expressed by Eq. (8.6) through the processes of Eqs. (8.3), (8.4), and (8.5).

$$V_1 = \frac{V}{s} - R_1 I - V_2 \quad (8)$$

$$= \frac{V}{s} - (C_2 R_1 s + \frac{R_1}{R_2} + 1) V_2 \quad (8.1)$$

$$= \frac{V}{s} - \frac{C_1 C_2 R_1 R_2 s + C_1 (R_1 + R_2)}{C_1 C_2 R_1 R_2 s^2 + (C_1 R_1 + C_2 R_2 + C_1 R_2) s + 1} V \quad (8.2)$$

$$= \frac{V}{s} - \frac{s + C_1 (R_1 + R_2) / (C_1 C_2 R_1 R_2)}{s^2 + [(C_1 R_1 + C_2 R_2 + C_1 R_2) / C_1 C_2 R_1 R_2] s + 1 / (C_1 C_2 R_1 R_2)} V \quad (8.3)$$

$$= \frac{V}{s} - \frac{s + C_1 (R_1 + R_2) / (C_1 C_2 R_1 R_2)}{(s - \alpha_1)(s - \alpha_2)} V \quad (8.4)$$

$$= \frac{V}{s} - \frac{1}{\alpha_1 - \alpha_2} \left(\frac{\alpha_1}{s - \alpha_1} - \frac{\alpha_2}{s - \alpha_2} \right) - \frac{C_1 (R_1 + R_2)}{C_1 C_2 R_1 R_2 (\alpha_1 - \alpha_2)} \left(\frac{1}{s - \alpha_1} - \frac{1}{s - \alpha_2} \right) V \quad (8.5)$$

$$= \frac{V}{s} - \frac{1}{\alpha_1 - \alpha_2} \left\{ \left[\alpha_1 + \frac{C_1 (R_1 + R_2)}{C_1 C_2 R_1 R_2} \right] \frac{1}{s - \alpha_1} - \left[\alpha_2 + \frac{C_1 (R_1 + R_2)}{C_1 C_2 R_1 R_2} \right] \frac{1}{s - \alpha_2} \right\} \quad (8.6)$$

By using inverse Laplace transform, Eq. (8.6) is given by

$$V_1 = Vu(t) + \frac{1}{\alpha_2 - \alpha_1} \left\{ \left[\alpha_1 + \frac{C_1 (R_1 + R_2)}{C_1 C_2 R_1 R_2} \right] e^{\alpha_1 t} - \left[\alpha_2 + \frac{C_1 (R_1 + R_2)}{C_1 C_2 R_1 R_2} \right] e^{\alpha_2 t} \right\} Vu(t) \quad (9)$$

Although $a_1 + a_2$ and $a_1 a_2$ are simply achievable from Eq. (8.3) as shown in Eq. (10), some approximation ($C_2 > C_1, R_2 > R_1$, and $a_2 > a_1$) makes the solution much simpler.

$$\alpha_1 + \alpha_2 = -\frac{(C_1 R_1 + C_2 R_2 + C_1 R_2)}{C_1 C_2 R_1 R_2}, \quad \alpha_1 \alpha_2 = \frac{1}{C_1 C_2 R_1 R_2} \quad (10)$$

$$\alpha_1 + \alpha_2 = -\frac{C_1 + C_2}{C_1 C_2 R_1}, \quad \alpha_1 \alpha_2 = \frac{1}{C_1 C_2 R_1 R_2} \quad (11)$$

$$\Rightarrow \alpha_2 = -\frac{1}{(C_1 + C_2) R_2}, \quad \alpha_1 = -\frac{C_1 + C_2}{C_1 C_2 R_1}$$

As the capacitance and resistance of drift term (C_2, R_2) are much larger than that of rapid changing term (C_1 and R_2), a_1 and a_2 of Eq. (11) is obtained and the effective gate volage of the gate node (V_G of Fig. 6) is expressed by Eq. (13) through Eq. (12).

$$V_1 = Vu(t) + \frac{1}{\alpha_2 - \alpha_1} \left\{ \frac{C_1 R_1 - C_2 R_2}{C_1 C_2 R_1 R_2} e^{\alpha_1 t} - \frac{1}{C_2 R_1} e^{\alpha_2 t} \right\} Vu(t) \quad (12)$$

$$V_G \cong \left[1 - \frac{C_2}{C_1 + C_2} e^{-(C_1 + C_2)t / C_1 C_2 R_1} - \frac{C_1}{C_1 + C_2} e^{-t / (C_1 + C_2) R_2} \right] Vu(t) \quad (13)$$

The response of the $V_G(t)$ to the step function input $V_{LG} u(t)$, where $u(t)$ is the unit step function ($u(t) = 1$ for $t > 0$ and $u(t) = 0$ for $t < 0$), is given as

$$V_G(t) = [1 - A_S e^{-t/\tau_S} - A_L e^{-t/\tau_L}] V_{LG} u(t) \quad (14)$$

where A_S and A_L are constants determined by the circuit parameters (R_1, R_2, C_1 , and C_2). The exponentially decaying function with a long time constant (τ_L) is the cause of the current drift. As far as the slow drift of current is concerned, we can ignore the effect of the exponential function with the short time constant (τ_S) since it decays quickly. It will appear just like a part of the step function. The physical meaning and notation of the parameters in Eq. (14) are summarized in tables of Fig. 7(a) and (b).

Although the drift effect is caused by the drift of the V_G , it cannot be measured directly. Thus, the I_D calculated by the proposed model needs to be compared with the measured I_D to verify the validity of the proposed model. For the I_D calculation, the operation region of the SiNW sensor was first confirmed. Fig. 8(a) shows the output characteristics to find the operation region of the device. It is confirmed that the SiNW sensor is operated in saturation mode ($V_{LG}/V_D = 1$ V). In the saturation mode ($V_G(t) - V_{th} < V_D$), the I_D is given by

$$I_D = \beta [V_G(t) - V_{th}]^2 / 2, \quad \text{for } V_G(t) - V_{th} > 0 \quad (15)$$

where β and V_{th} represent the gain factor and threshold voltage of the FET, respectively. Fig. 8(b) shows that the $I_D - V_{LG}$ characteristic was measured with a long integration time of 15 s at each step to extract the saturated I_D (meaning the drift-free I_D because the I_D is measured after the I_D drift is finished) as a function of the V_{LG} . By substituting the extracted relationship between the drift-free I_D

(a)			(b)		
Notation	Component	Reaction rate	Notation	Components	Physical meaning
C_1	Gate capacitance without H ⁺ movement	Fast response	τ_L	$(C_1 + C_2) R_2$	long time constant
R_1	Resistance of electrolyte		τ_S	$C_1 C_2 R_1 / (C_1 + C_2)$	short time constant
C_2	Gate capacitance with H ⁺ movement	Slow response	A_L	$\frac{C_2}{C_1 + C_2}$	initial state for τ_L
R_2	Resistance of H ⁺ at oxide		A_S	$\frac{C_1}{C_1 + C_2}$	initial state for τ_S

$D_{eff}(H^+) \sim 10^{-23} \text{ cm}^2/\text{s}$ at 300K (pure oxide) * $R_2 \gg R_1$
 $D_{eff}(H^+) \sim 10^{-18} \text{ cm}^2/\text{s}$ at 300K (defective oxide)

Fig. 7. (a) Parameters for electrical circuit model. (b) Notations for simple expression and its components/physical meaning.

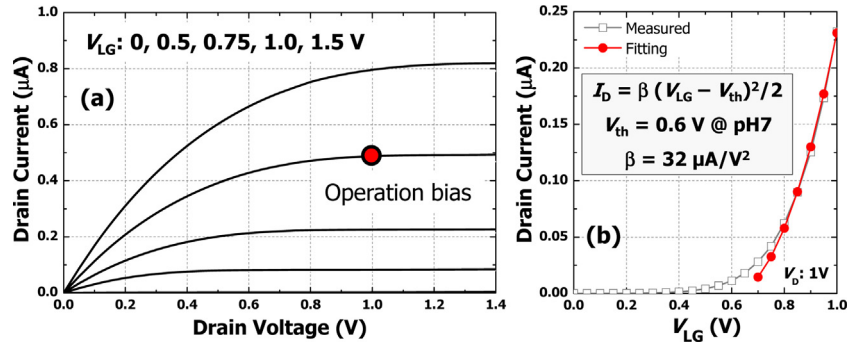


Fig. 8. (a) Measured output characteristics at various V_{LG} s. (b) Transfer characteristic with long integration time of 15 s at each step. Calculated I_D by equation of inset is fitted to measured I_D with long integration time to obtain gain factor (β).

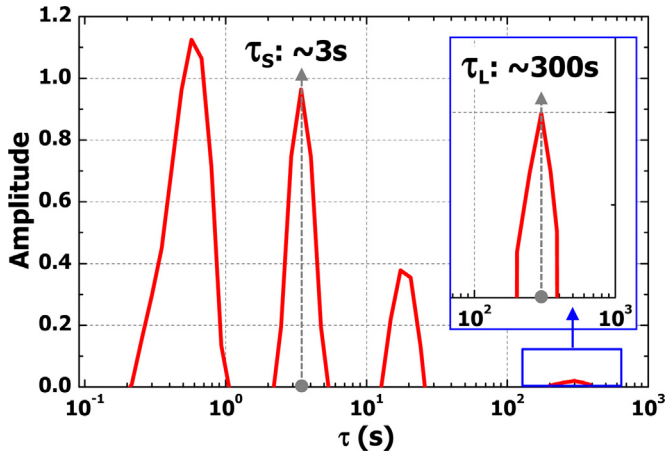


Fig. 9. Time-constant spectrum extracted by fitting calculated I_D to measured I_D using Eqs. (15) and (17).

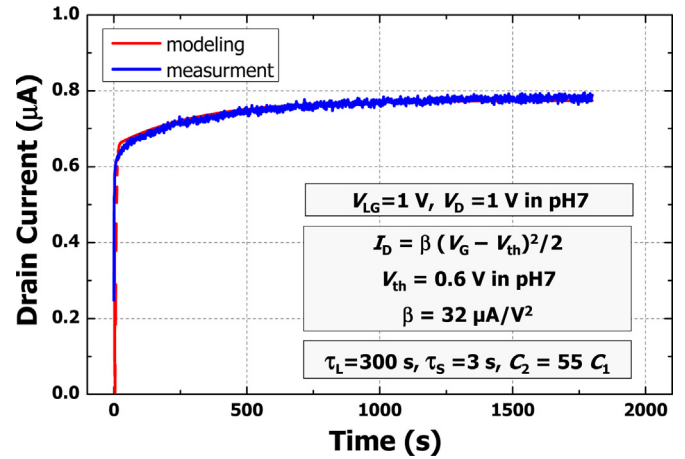


Fig. 10. Comparison of measured I_D and calculated I_D by using proposed model and calibrated parameters.

and the V_{LG} into Eq. (15), we can obtain the constant $\beta = 32 \mu\text{A/V}^2$ as shown in Fig. 8(b).

The Eq. (16) demonstrates that the V_G of Eq. (14) can be converted to the I_D by substituting Eq. (14) into Eq. (15) with the calibrated β .

$$I_D = \beta \{ [(1 - A_S e^{-t/\tau_S} - A_L e^{-t/\tau_L}) V_{LG}(t) - V_{th}]^2 / 2, \text{ for } V_G(t) - V_{th} > 0 \quad (16)$$

$$\beta = 32 \mu\text{A/V}^2$$

Moreover, A_S , A_L , τ_S , and τ_L in Eq. (16) were determined by the optimized process. The I_D with the drift is analyzed by fitting it using Eqs. (15) and (17), which models the increased current as the sum of pure single exponential terms [28]:

$$V_G(t) = [1 - \sum_{n=1}^N A_n \exp(-t/\tau_n)] V_{LG}(t) \quad (17)$$

Each single exponential term means the change in the I_D influenced by the I_D drift with the time constant τ_n . The fitting is performed to minimize the sum of $|\text{measured } I_D - \text{calculated } I_D|^2$ at the measured points. In this process, A_n 's are the fitting parameters to be evaluated, whereas τ_n 's are the predefined constants. A total of 85 single exponential terms with time constants τ_n , which are equally spaced logarithmically in time, are used for fitting the experimental result. Fig. 9 shows the extracted time-constant spectrum where 3 s and 300 s can be determined as τ_S and τ_L , respectively. Also, the relation of $C_2 = 55C_1$ can be extracted from the amplitudes of the selected τ_S and τ_L .

Consequently, Fig. 10 reveals that the proposed model consisting of only electrical circuit components reflects the drift effect

related to the H^+ movement by using the calibrated parameters such as $\beta = 32 \mu\text{A/V}^2$, $C_2 = 55C_1$, $\tau_S = 3 \text{ s}$, and $\tau_L = 300 \text{ s}$.

4. Conclusions

In this study, the SiNW sensor was co-integrated with the CMOS circuit by using top-down approach and CMOS-compatible back-end process. To investigate the physical origin of the I_D drift, the transient I_D characteristics of the fabricated SiNW sensor were monitored with various V_{LG} s and pH values. It is revealed that the field-enhanced H^+ penetration through the defective sensing insulator causes the I_D drift. For the application of the SiNW sensor to integrated circuits, we propose the electrical model which can reflect the drift effect and can be expressed only by the combination of electrical circuit components. In the proposed model, R_1 represents the resistance of the electrolyte and the FET can be approximated by the capacitances C_1 (capacitance of pure gate oxide in which hydrogen ions move very slowly) and C_2 (capacitance by gate oxide with defects in which hydrogen ions move relatively faster). Furthermore, the movement of H^+ in the defective oxide is represented by R_2 and the current drift is modeled as the parallel combination of the C_2 and the R_2 because the drift effect is strongly related to the H^+ movement through the defective gate oxide. Consequently, the SiNW sensor with the I_D drift can be modeled by the series connection of the R_1 , the parallel combination of the C_2 and the R_2 , and the C_1 . The calculated I_D by the proposed model is successfully fitted to the measured time-dependent I_D of the SiNW sensor.

Acknowledgements

This work was supported by the Brain Korea 21 Plus Project in 2016 and in part by the National Research Foundation of Korea (NRF) funded by the Korean Government under Grant 2013R1A1A2065339, 2016R1A5A1012966, and 2016R1A6A3A01006588.

References

- [1] M.-C. Cheng, G. Cuda, Y.L. Bunimovich, M. Gaspari, J.R. Heath, H.D. Hill, C.A. Mirkin, A.J. Nijdam, R. Terracciano, T. Thundat, M. Ferrari, Nanotechnologies for biomolecular detection and medical diagnostics, *Curr. Opin. Chem. Biol.* 10 (2006) 11–19.
- [2] N.C. Tansil, Z. Gao, Nanoparticles in biomolecular detection, *Nano Today* 1 (2006) 28–37.
- [3] R.J. Lipshutz, S.P.A. Fodor, T.R. Gingeras, D.J. Lockhart, High density synthetic oligonucleotide arrays, *Nature Genet.* 21 (1999) 20–24.
- [4] M. Curreli, R. Zhang, F.N. Ishikawa, H.K. Chang, R.J. Cote, C. Zhou, M.E. Thompson, Real-time, label-free detection of biological entities using nanowire-based FETs, *IEEE Trans. Nanotechnol.* 7 (2008) 651–667.
- [5] Q. Cui, H. Wei, C.M. Park, Lieber, Nanowire nanosensors for highly sensitive and selective detection of biological and chemical species, *Science* 293 (2001) 1289–1292.
- [6] G. Zheng, F. Patolsky, Y. Cui, W.U. Wang, C.M. Lieber, Multiplexed electrical detection of cancer markers with nanowire sensor arrays, *Nat. Biotechnol.* 23 (2005) 1294–1301.
- [7] F. Patolsky, G. Zheng, O. Hayden, M. Lakadamyali, X. Zhuang, C.M. Lieber, Electrical detection of single viruses, *PNAS* 101 (2004) 14017–14022.
- [8] F. Patolsky, G. Zheng, C.M. Lieber, Fabrication of silicon nanowire devices for ultrasensitive, label-free, real-time detection of biological and chemical species, *Nature Protocol* 1 (2006) 1711–1724.
- [9] K.E. Stern, J.F. Klemic, D.A. Routenberg, P.N. Wyrembak, D.B. Turner-Evans, A.D. Hamilton, D.A. LaVan, T.M. Fahmy, M.A. Reed, Label-free immune detection with CMOS-compatible semiconducting nanowire, *Nature* 445 (2007) 519–522.
- [10] A. Kim, C.S. Ah, H.Y. Yu, J.-H. Yang, I.-B. Baek, C.-G. Ahn, C.W. Park, M.S. Jun, Ultrasensitive, label-free, and real-time immune detection using silicon field-effect transistors, *Appl. Phys. Lett.* 91 (2007) 103901.
- [11] K.-S. Shin, K. Lee, J.Y. Kang, C.O. Chui, Novel T-channel nanowire FET built-in signal amplification for pH sensing, *IEDM Tech. Dig.* (2009) 599–602.
- [12] C.-Y. Hsiao, C.-H. Lin, C.-H. Hung, C.-J. Su, Y.-R. Lo, C.-C. Lee, H.-C. Lin, F.-H. Ko, T.Y. Huang, Y.-S. Yang, Novel poly-silicon nanowire field effect transistor for biosensing application, *Biosens. Bioelectron.* 24 (2009) 1223–1229.
- [13] A. Gao, N. Lu, P. Dai, T. Li, H. Pei, X. Gao, Y. Gong, Y. Wang, C. Fan, Silicon-nanowire-based CMOS-compatible field-effect transistor nanosensors for ultrasensitive electrical detection of nucleic acids, *Nano Lett.* 11 (2011) 3974–3978.
- [14] Y.-Z. Juang, C.-F. Lin, H.-H. Tsai, Y.-K. Su, R.-L. Wang, W.-L. Li, P.-C. Kung, A fully compatible CMOS-based hydrogen ion sensor using natural forming sensing membrane for urea detecting application, *Procedia Chem.* 1 (2009) 1067–1070.
- [15] P. Ginet, S. Akiyama, N. Takama, H. Fujita, B. Kim, CMOS-compatible fabrication of top-gated field-effect transistor silicon nanowire-based biosensors, *J. Micromech. Microeng.* 21 (2011) 065008.
- [16] W.-Y. Chung, F.G. Cruz, C.-H. Yang, F.-S. He, T.-T. Liu, D.G. Pijanowska, W. Torbicz, P.B. Grabiec, B. Jarosewicz, CMOS Readout Circuit Developments for Ion Sensitive Field Effect Transistor Based Sensor Applications, *Solid State Circuits Technologies*, Intech, Croatia, 2010, pp. 421–444.
- [17] I. Park, Z. Li, A.P. Pisano, R.S. Williams, Top-down fabricated silicon nanowire sensors for real-time chemical detection, *Nanotechnology* 21 (2009) 015501.
- [18] O.V. Naumova, B.I. Fomin, D.A. Nasimov, N.V. Dudchenko, S.F. Devyatova, E.D. Zhanaev, V.P. Popov, A.V. Latyshev, A.L. Aseev, Y.D. Ivanov, A.I. Archakov, SOI nanowires as sensors for charge detection, *Semicond. Sci. Technol.* 25 (2010) 055004.
- [19] J. Lee, J.M. Lee, J.H. Lee, M. Uhm, W.H. Lee, S. Hwang, I.Y. Chung, B.G. Park, D.M. Kim, Y.J. Jeong, D.H. Kim, SiNW-CMOS hybrid common-source amplifier as a voltage-readout hydrogen ion sensor, *IEEE Electron Device Lett.* 34 (2013) 135–137.
- [20] J. Lee, J.M. Lee, J.H. Lee, W.H. Lee, M. Uhm, B.G. Park, D.M. Kim, Y.J. Jeong, D.H. Kim, Complementary silicon nanowire hydrogen ion sensor with high sensitivity and voltage output, *IEEE Electron Device Lett.* 33 (2012) 1768–1770.
- [21] D.W. Kwon, J.H. Lee, S. Kim, R. Lee, H. Mo, J. Park, D.H. Kim, B.G. Park, Drift-Free pH Detection With Silicon Nanowire Field-Effect Transistors, *IEEE Electron Device Lett.* 37 (2016) 652–655.
- [22] S. Martinoia, G. Massobrio, A Behavioral macromodel of the ISFET in SPICE, *Sens. Actuators B: Chem.* 62 (2000) 182–189.
- [23] W.-W. Chung, F.-S. He, C.-H. Yang, M.-C. Wang, Drift response macromodel and readout circuit development for ISFET and its H⁺ sensing applications, *J. Med. Biol. Eng.* 26 (2005) 29–34.
- [24] L. Bousse, P. Bergveld, The role of buried oh sites in the response mechanism of inorganic-gate pH-sensitive ISFETs, *Sens. Actuators* 6 (1984) 65–78.
- [25] P. Woias, L. Meixner, P. Fröstl, Slow pH response effects of silicon nitride ISFET sensors, *Sens. Actuators B: Chem.* 48 (1998) 501–504.
- [26] S. Jamasb, S.D. Collins, R.L. Smith, A physical model for drift in pH ISFETs, *Sens. Actuators B: Chem.* 49 (1998) 146–155.
- [27] S. Jamasb, S.D. Collins, R.L. Smith, A physical model for threshold voltage instability in Si₃N₄-Gate H⁺-sensitive FETs (pH-ISFETs), *IEEE Trans. Electron Devices* 45 (1998) 1239–1245.
- [28] J. Joh, J. del Alamo, A current-transient methodology for trap analysis for GaN high electron mobility transistors, *IEEE Trans. Electron Devices* 58 (2011) 132–140.

Biographies

Dae Woong Kwon received Ph.D. degrees in Electrical Engineering at Seoul National University (SNU), Seoul, Korea, in 2017. He had designed nand flash memory devices from 2005 to 2014 at Samsung Electronics, Yongin, Korea. His current research interests include tunnel FET, bio-sensor, nand flash memory, metal oxide thin-film transistors, and negative capacitance FET.

Sihyun Kim received the B.S. degree in 2014 from Seoul National University (SNU), Seoul, Korea. He is currently working toward the Ph. D. degree in electrical engineering from Seoul National University (SNU), Seoul, Korea. His research interests include silicon nanowire biosensors and tunnel field-effect transistor (TFET).

Ryoongbin Lee received the B.S. degree in 2014 from SungKyunKwan University (SKKU), Suwon, Korea. He is currently working toward the Ph. D. degree in electrical engineering from Seoul National University (SNU), Seoul, Korea. His research interests include silicon nanowire biosensors and tunnel field-effect transistor (TFET).

Hyun-Sun Mo received the B.S., M.S., and Ph.D degrees in Electronic Engineering from Kookmin University, Seoul, Korea, in 1993 and 2011, and 2014, respectively. In 1993, she joined Samsung Electronics Semiconductor Division of the development of the low power and high-speed SRAM and Flash memory circuits. Her research interests include the design of analog circuits, power-management ICs, and the next-generation memories.

Dae Hwan Kim received the B.S., M.S., and Ph.D. degrees in electrical engineering from Seoul National University, Seoul, Korea, in 1996, 1998, and 2002, respectively. He is currently an Associate Professor with the School of Electrical Engineering, Kookmin University, Seoul, Korea. His current research interests include nanoCMOS, oxide and organic thin-film transistors, biosensors, and neuromorphic devices.

Byung-Gook Park received the B.S. and M.S. degrees in electronic engineering from Seoul National University (SNU), Seoul, Korea, in 1982 and 1984, respectively, and the Ph.D. degree in electrical engineering from Stanford University, Stanford, CA, USA, in 1990. He joined the School of Electrical Engineering, SNU, in 1994, as an Assistant Professor, where he is currently a Professor. He holds more than 100 Korean and U.S. patents.